ADVANCED MATERIALS
www.advmat.de

Quantum-Confinement-Enhanced Thermoelectric Properties in Modulation-Doped GaAs–AlGaAs Core–Shell Nanowires

*Sergej Fust, Anton Faustmann, Damon J. Carrad, Jochen Bissinger, Bernhard Loitsch, Markus Döblinger, Jonathan Becker, Gerhard Abstreiter, Jonathan J. Finley, and Gregor Koblmüller**

Nanowires (NWs) hold great potential in advanced thermoelectrics due to their reduced dimensions and low-dimensional electronic character. However, unfavorable links between electrical and thermal conductivity in state-of-the-art unpassivated NWs have, so far, prevented the full exploitation of their distinct advantages. A promising model system for a surface-passivated one-dimensional (1D)-quantum confined NW thermoelectric is developed that enables simultaneously the observation of enhanced thermopower via quantum oscillations in the thermoelectric transport and a strong reduction in thermal conductivity induced by the core–shell heterostructure. High-mobility modulation-doped GaAs/AlGaAs core–shell NWs with thin (sub-40 nm) GaAs NW core channel are employed, where the electrical and thermoelectric transport is characterized on the same exact 1D-channel. 1D-sub-band transport at low temperature is verified by a discrete stepwise increase in the conductance, which coincided with strong oscillations in the corresponding Seebeck voltage that decay with increasing sub-band number. Peak Seebeck coefficients as high as ≈65–85 μV K^{-1} are observed for the lowest sub-bands, resulting in equivalent thermopower of $S^2\sigma \approx 60$ μW m^{-1} K^{-2} and $S^2G \approx 0.06$ pW K^{-2} within a single sub-band. Remarkably, these core–shell NW heterostructures also exhibit thermal conductivities as low as ≈3 W m^{-1} K^{-1}, about one order of magnitude lower than state-of-the-art unpassivated GaAs NWs.

Thermoelectric materials, which convert temperature gradients into electricity or pump heat by electricity, have attracted a lot of attention for applications in waste heat recovery for power generation and in solid-state refrigeration.[1] The prime challenge in this area is to improve the energy conversion efficiency, which requires suitable materials with large thermoelectric power factor ($S^2\sigma$), high electrical conductivity (σ) to suppress Joule heating, and low thermal conductivity (κ) to enable large temperature gradients and prevent heat dissipation at the device junctions.[1,2] Optimization of these relevant parameters presents, however, tremendous challenges due to the unfavorable coupling between most of these quantities. In particular, in bulk-like materials the Seebeck coefficient S depends on carrier density and is inversely proportional to the electrical conductivity, while the electrical conductivity and the electronic part of the thermal conductivity are interrelated via the Wiedemann–Franz law.[3]

A promising approach to decouple these interdependencies is brought by nanostructuring thermoelectric materials, as pioneered theoretically by Hicks and Dresselhaus.[4,5] Reducing size dimensions to much smaller than the phonon mean free path enhances phonon scattering, which reduces the lattice contributions to the thermal conductivity.[1] Likewise, improvements in thermopower are expected by exploitation of the quantum-confinement enhanced electronic density of states in low-dimensional semiconductor systems.[4–6] In this regard, one-dimensional (1D) nano- or quantum-wires are very appealing, especially if they can host 1D-like charge carrier channels with high carrier mobility and small nanowire (NW) cross-sections.[6,7] Numerous efforts were undertaken to demonstrate reductions in thermal conductivity in NWs,[8–11] while much less emphasis has been directed to explore the effects of 1D quantum confinement on enhancements in thermopower $S^2\sigma$ of high-mobility semiconductor NWs. InAs NWs receive the most attention out of the various candidate materials, with discrete conductance steps[7,12–14] and Seebeck coefficient oscillations in thin NWs with diameter ≈20–60 nm observed.[7,13] However, these results were obtained in the nonballistic—, i.e., diffusive—limit, which limits the magnitude of the extracted thermopower.[7] This is unsurprising, given the common defect distributions in NWs

S. Fust, A. Faustmann,[+] Dr. D. J. Carrad,[++] J. Bissinger, Dr. B. Loitsch, J. Becker, Prof. G. Abstreiter, Prof. J. J. Finley, Dr. G. Koblmüller
Walter Schottky Institut and Physik Department
Technical University of Munich
Am Coulombwall 4, 85748 Garching, Germany
E-mail: Gregor.Koblmueller@wsi.tum.de
Dr. M. Döblinger
Department of Chemistry
Ludwig-Maximilians-University Munich
Butenandtstr. 11, 81377 Munich, Germany
The ORCID identification number(s) for the author(s) of this article can be found under https://doi.org/10.1002/adma.201905458.

[+]Present address: Peter Grünberg Institut (PGI-9), Forschungszentrum Jülich, 52425 Jülich, Germany
[++]Present address: Center for Quantum Devices, Niels Bohr Institut, University Copenhagen, Universitetsparken 5, 2100 Copenhagen, Denmark

DOI: 10.1002/adma.201905458

and the increased surface scattering in unpassivated InAs NWs which inhibits high mobility.[15,16] Hence, the deployed strategies to reduce the diameters of NWs to the 1D confinement regime, which is beneficial for increased phonon scattering,[17,18] do not necessarily come with improved thermopower. The fact that the electrical and thermal properties remain unfavorably linked in InAs NWs encourages the development of different approaches that simultaneously provide thermopower enhancement in 1D-confined high-mobility channels at substantially reduced thermal conductivity. In this work, we demonstrate that modulation-doped core–shell NWs, illustrated here for the prototypical Si delta-doped GaAs–AlGaAs materials system produced by bottom-up synthesis, can hold such promising potential. In particular, our investigation shows that transport occurs via discrete 1D-modes confined to the NW core, with conductance plateaus and steps correlated to thermopower oscillations. Extracted Seebeck coefficients for the first few 1D-sub-bands are on the order of several tens of $\mu V\ K^{-1}$ and peaks at around ≈65–85 $\mu V\ K^{-1}$ for the two lowest sub-bands. Analysis of the thermal conductivity was further performed by micro-Raman spectroscopy, demonstrating that the advanced core–shell GaAs–AlGaAs NW heterostructures exhibit thermal conductivities as low as ≈3 $W\ m^{-1}\ K^{-1}$, i.e., up to an order of magnitude lower than those commonly found in unpassivated GaAs NWs.

The radially modulation-doped GaAs–AlGaAs core–shell NWs were fabricated in a three-step growth process on prepatterned SiO_2/Si (111) substrates by molecular beam epitaxy (MBE). Initially, the GaAs NW core was grown along the vertical [111] orientation via an autocatalytic (i.e., Ga-droplet assisted) vapor–liquid–solid (VLS) growth process, yielding nominally ≈7–10 μm long cores with typical diameters of >60 nm.[19–21] In order to allow the observation of a set of discrete sub-bands with sufficiently large energy level spacing, quantum confinement effects demand the diameter of the core channel to be relatively thin, i.e., < 40 nm.[22] Hence, in a second step the GaAs core was thinned by a reverse-reaction growth step (i.e., in situ annealing) at elevated temperature (680 °C) for 80 min. This process enables the realization of ultrathin GaAs cores with diameters even below 20 nm, while the length also decreases due to competitive thermal decomposition processes of the participating {1-10} and {111} NW facets.[23] Subsequently, in the third step, the thinned GaAs core was overgrown radially by a closely lattice-matched AlGaAs shell layer (x(Al) ≈ 0.15%) with a total thickness of ≈80 nm, and a final 5 nm thin GaAs cap layer. At about 20 nm separation from the GaAs/AlGaAs core–shell interface a Si δ-doped layer was implemented using a doping density of $\approx 6 \times 10^{19}\ cm^{-3}$ as confirmed by previous atom probe tomography studies.[19,22] The δ-doping thereby enables the realization of a high-mobility, high-carrier density electron channel confined to the NW core with low-temperature electron mobilities up to $5 \times 10^3\ cm^2\ V^{-1}\ s^{-1}$ at average carrier densities of $(\approx 5–10) \times 10^{17}\ cm^{-3}$.[19]

Figure 1 shows an overview scanning electron microscopy (SEM) image of the final NWs as-grown on Si (111) substrate, as well as a schematic cross-section of the Si δ-doped GaAs/AlGaAs core–shell NW heterostructure (inset). The final NWs have a length of ≈4–6 μm and they exhibit total diameters of around ≈200 nm without any tapering. Subsequent cross-sectional analysis using atomic force microscopy (AFM) and scanning helium ion microscopy (SHeIM) (see Figure 1b) confirmed the SEM-measured NW diameter. The contrast between GaAs and AlGaAs, as well as the presence of Al-rich stripes at the corner facets in cross-sectional SHeIM analysis, allowed us to further determine the core diameter and shell thickness, in analogy to our recent work on SHeIM of radial NW-heterostructures.[24] Specifically, the NW cross-section presented in Figure 1b exhibits a GaAs core diameter of ≈35 nm and an AlGaAs shell thickness of ≈75 nm. Analysis of several NW cross-sections found that, in general, the GaAs core diameter varied between ≈15–40 nm, while the AlGaAs shell was fairly homogeneous with a fixed thicknesses of ≈75–80 nm, close to the nominally expected value. To determine the underlying crystal structure, high-resolution transmission electron microscopy was performed on an NW reference grown under identical conditions. As shown in the Supporting Information, the NWs consist of a pristine zinc-blende (ZB) crystal phase with few isolated rotational twin defects (≈0.2 twins μm^{-1}). Figure 1c further illustrates the central idea of the formation of a free electron gas confined to the GaAs core by the employed Si δ-doping scheme. In particular, the plot shows the profile of the conduction band (CB) over the GaAs–AlGaAs core–shell heterointerface, calculated at 4 K and zero bias via self-consistent solutions of the Schrödinger–Poisson equation using the commercial nextnano^3 device simulator.[19,22,25] Under the given geometry (30 nm thin GaAs core, 75 nm thick AlGaAs shell) and an equivalent Si δ-doping density of $6 \times 10^{19}\ cm^{-3}$,[19] the evolution of the CB profile clearly shows that the total electron charge carrier density is confined to the NW core (red region below the Fermi level E_F).

NWs were then transferred mechanically to prepatterned substrates, onto which specific test structures were fabricated to probe the electrical/thermoelectric transport and the thermal transport properties of single NWs separately. Most importantly, direct correlation between electrical conductivity and Seebeck effect is realized on the same exact single NW device as further shown below, while complementary comparison of thermal transport is achieved by statistical analysis of several individual NWs from the same growth sample. For further details regarding device fabrication of the two distinct test structures we refer to the Experimental Section, while representative devices for characterization of thermal conductivity as well as thermoelectric transport are displayed in **Figures 2** and 4, respectively.

First, we show thermal transport experiments performed on individual NWs carried out in a micro-Raman (μRaman) spectroscopy setup in backscattering geometry at room temperature, similar to recently reported experiments performed on carbon nanotubes and various different NW materials.[26–30] Hereby, a helium-neon laser with a wavelength of 632.8 nm was used to locally heat the NW in vacuum, whilst at the same time the backscattered Raman signal was observed that contains information about the local temperature that is necessary for the thermal conductivity determination.[28,29] Note that under the employed excitation conditions, light is absorbed in both the NW core and shell as their bandgaps are well below the incident photon energy (1.96 eV). To suppress heat propagation via the underlying substrate (Si wafer), individual NWs were freely suspended on ≈300 nm thick gold (Au) strips of equal spacing (3 μm).[28] Care was taken that from the

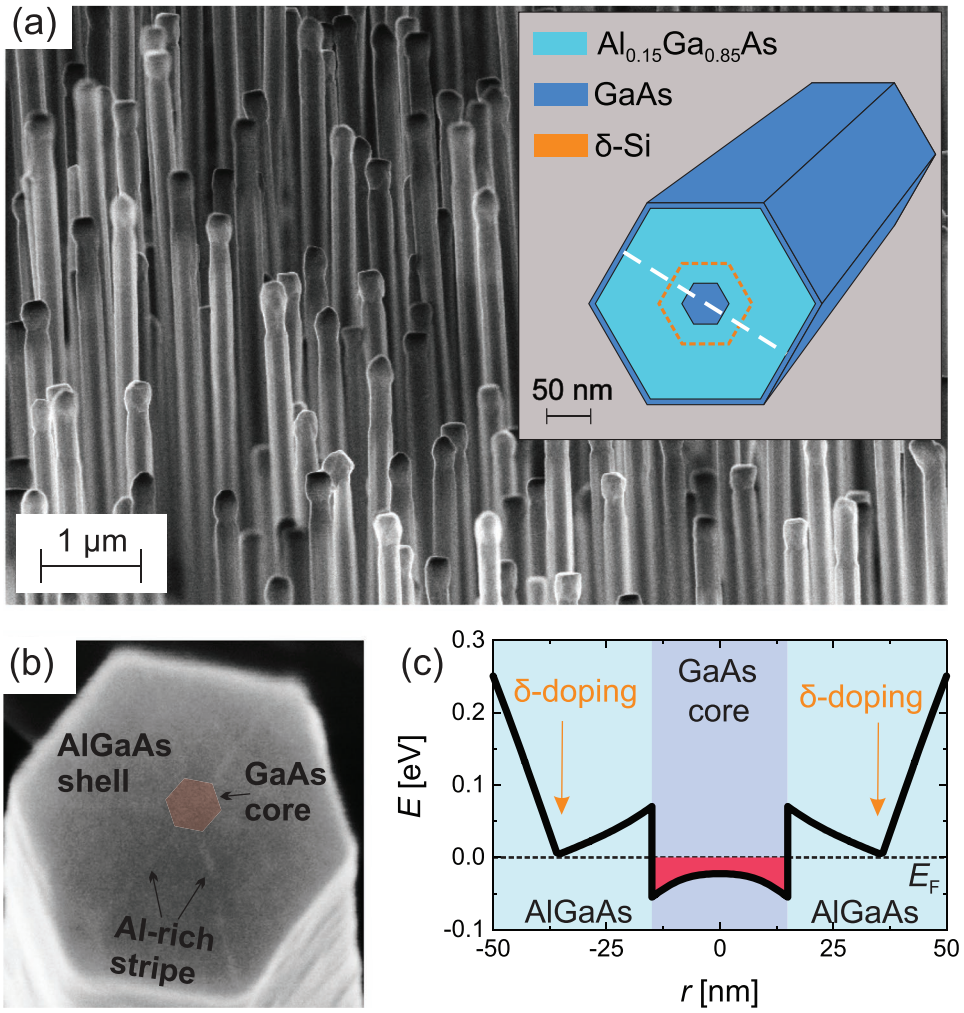

Figure 1. a) SEM image and schematic cross-section (inset) of modulation-doped GaAs–AlGaAs core–shell NWs as-grown on Si (111) substrate. b) SHeIM image (in false color) of a representative NW-cross-section, illustrating the thin GaAs core, the surrounding AlGaAs shell, and additional Al-rich stripes propagating along the {11-2} NW corner facets.[19,24] c) Calculated profile of the conduction band over the core–shell heterointerface (along major {1-10} orientation, as marked by white dashed line in inset of (a)) employing the nominal NW geometry and a Si doping density of 6×10^{19} cm^{-3};[19] charge separation between free electrons and spatially fixed ionized Si impurities (δ-doping layer) lead to band bending and formation of a confined electron gas in the NW core (red) (E_F represents the Fermi energy).

randomly dropcasted NWs only those were selected for measurements which bridge the Au strips orthogonally, separating them well from the Si substrate (see SEM image of Figure 2a) and acting as a heat sink. In total, three individual NWs with distinctly different diameters were probed in this way, under a configuration where the laser beam is incident on the {1-10} NW sidewall facets. To obtain statistically representative data, each NW was measured multiple times and their typical performance is shown in the Supporting Information. It is important to note that prior to the thermal transport measurements the NWs were first observed by optical microscopy, and only after the completed analysis, SEM was employed to determine the actual NW diameters. This guaranteed the intrinsic NW properties from being modified by the incident electron irradiation and common carbon contamination in SEM.[31]

Figure 2b shows two backscattered Raman spectra of a representative NW probed on the Au strips (black curve) and at a center position of the NW, furthest away from the strips (red curve). At a Raman wavenumber of 523 cm^{-1} we observe a strong peak, which stems from the Si-substrate. Regarding the signal from the NW, the normally dominating GaAs-like longitudinal optical mode is theoretically forbidden in this geometry, and is thus strongly suppressed, seen here only as a weak bump in the spectra at a wavenumber of about 290 cm^{-1}.[28] Hence, we focus our observations of the effects of local laser heating on the respective temperature change in the NW on the Raman shifts of the GaAs-like transverse optical (TO) mode.[28] When probed at or near the Au strip, this peak is centered at ≈267 cm^{-1}, inducing negligible temperature change at this position since the absorbed heat is dissipated very fast via the Au strip. By contrast, when the NW is irradiated in between the strips, heat transport can only occur via the NW. Thus, the local temperature in the NW increases, which shifts the GaAs TO phonon peak to lower wavenumbers, i.e., ≈265 cm^{-1} at the

central position of the NW (see inset of Figure 2b). A linear relation between the change in wavenumber and corresponding temperature gradient allows a temperature determination from the relative Raman shift,[28,32] by $d\omega/dT = -0.016$ cm^{-1} K^{-1}. This relationship is insensitive to changes in NW size, as confirmed by studies of Si bulk and NWs over large diameter ranges down to 30 nm.[27]

Figure 2d shows the obtained temperature profiles for three individual NWs when scanned at equidistant positions of ≈200 nm along the NW under similar excitation laser power (100–140 μW). We note that measurements performed under slightly different laser power (range of 95–170 μW) had no measurable effect on the resulting thermal conductivity. According to AFM and SEM analysis, the total cross-sectional diameters of the three NWs were 175 ± 2 nm (NW-1), 185 ± 2 nm (NW-2), and 195 ± 2 nm (NW-3), respectively. This variation in total NW diameter stems primarily from slight variations of the core diameter (≈15–35 nm) while the AlGaAs shell thickness is rather constant at ≈75 nm. As a consequence, we find that with increasing total NW diameter the induced local temperature change becomes smaller. This is expected, since with increasing NW diameter more volume is heated, while the irradiated area increases only marginally. Consecutively, each temperature profile along the NW was fitted, according to an established model for diffusive heat transport along a suspended 1D wire.[26,28] Hereby, the change in temperature is characterized by a parabola with negative curvature, which generates a fitting parameter $f = \kappa A/P_{abs}$. This expression contains the thermal conductivity κ, the total cross-section A of the NW (i.e., core + shell) and the absorbed laser power P_{abs}. For the latter, P_{abs} is defined by the product of the measured laser power and an absorption factor which is highly dependent on the NW diameter, the refractive index and the excitation wavelength. Furthermore, we incorporate a Gaussian-shaped laser spot into our model to enable fully quantitative comparison with unpassivated GaAs NWs.[28] The fraction of the laser power absorbed by the NW was simulated using finite-difference-time-domain (FDTD) simulations (Lumerical). We find that, depending on the NW diameter, the fraction of the light absorbed by the NW waveguide with respect to the total amount of incident light varies between 10% and 25%, showing an absorption resonance at a diameter of 190 nm at the incident wavelength of 632 nm (see Figure 2c). The insets illustrate examples of the total absorption at the incident wavelength for NWs with diameters both on- and off-resonance. With the information of the NW cross-section and the calculated absorbed laser power, we can directly extract the thermal conductivity from the fitting parameter.

The extracted thermal conductivity data are summarized in **Figure 3** and further compared with literature data of unpassivated GaAs NWs as well as bulk (Al)GaAs material. Quite remarkable, we find very low thermal conductivity in the modulation-doped GaAs–AlGaAs core–shell NWs, which lie in the range of ≈3–5 (±0.5) W m^{-1} K^{-1} for two of the investigated NWs. The third NW (diameter 195 nm), has a slightly higher thermal conductivity of ≈10 (±2) W m^{-1} K^{-1}. On average, these values are about one order of magnitude lower as compared to n-type bulk GaAs (≈40–54 W m^{-1} K^{-1} at [n]~10^{16}–10^{18} cm^{-3}) at room temperature.[33] Further comparison with experimental data on unpassivated GaAs NWs (diameters ≈150–170 nm) as measured under similar conditions, show that they exhibit much higher values (≈20–36 W m^{-1} K^{-1})[28] than the present core–shell NWs. Note that the structural properties of previously reported unpassivated GaAs NWs are similar to the present core–shell NWs, exhibiting pristine ZB crystal phase with few twin defects.[28] Hence, we can rule out that the reduction in thermal conductivity of the core–shell NWs is influenced by the microstructure, although, in principle, modifications in crystal phase, e.g., different polytypes, or high densities of stacking defects can affect thermal conductivity quite strongly as observed in other III–V NW systems.[34,35] This confirms that, with NW diameters and crystal structure of unpassivated and passivated NWs being quite similar, the strong inhibition in thermal transport must arise from the specific core–shell NW heterostructure. Tentatively, we attribute the substantially reduced thermal conductivity of our GaAs–AlGaAs core–shell NWs to i) effective alloy scattering induced by the ternary AlGaAs shell, and ii) to phonon boundary scattering via the core–shell NW geometry. Considering alloy scattering, indeed, a large portion of the NWs consists of AlGaAs (>80% of the total NW volume). The thermal conductivity of AlGaAs is highly sensitive to the Al molar fraction, with a bulk value of ≈20–30 W m^{-1} K^{-1} for an Al molar fraction of x(Al) ≈0.15 as used in our NWs,[36] which is at least a factor of ≈2–3 lower than bulk GaAs. Furthermore, ordering effects beyond the random alloy limit may also affect the lattice thermal conductivity.[37] Radial GaAs–AlGaAs core–shell NWs are well known to exhibit such ordering effects, e.g., alloy clusters (i.e., nanodots ≈1–10 nm in size) as well as sixfold Al-enriched layers along the {11-2} corner facets in the AlGaAs shell are observed (see Figure 1b).[24,38] However, for such effects to contribute to phonon scattering below the AlGaAs alloy limit, very short-period ordering with large Al/Ga-compositional variations are required.[39,40]

The more substantial reduction in thermal conductivity is expected to stem, however, from the specific core–shell geometry. Recent theoretical work performed on core–shell NW systems with a high-κ core and low-κ shell material (e.g., Si–SiGe core–shell NWs)[41–43] exhibited large reductions in thermal conductivity due to diffusive phonon boundary scattering at the core–shell interface. In particular, as suggested by Hu et al.[42] the thermal conductivity drops rapidly in core–shell NWs with decreasing NW diameter, especially in regimes where ballistic phonon transport can be neglected. Similar trend is seen also by our data, i.e., by reducing the overall diameter (and with that the relative ratios of core-to-shell thickness) we found a successive reduction in κ from ≈10 to ≈3 W m^{-1} K^{-1}. In the limit of very small GaAs cores it has to be also considered that optical phonon confinement effects beyond the diffusive phonon boundary scattering may contribute to further lowering of thermal conductivity.[44] This effect, however, is expected to only occur in GaAs for size dimensions lower than ≈ 10 nm.[45] Moreover, mismatch of phonon spectra and corresponding changes in phonon group velocities,[46] as well as coherent phonon resonance effects[47] may also be considered in thermal conductivity reductions in core–shell geometries. This motivates for comprehensive modeling efforts along with systematic parameter variations (tuning alloy composition, size confinement, interface/surface roughness engineering, etc.) to

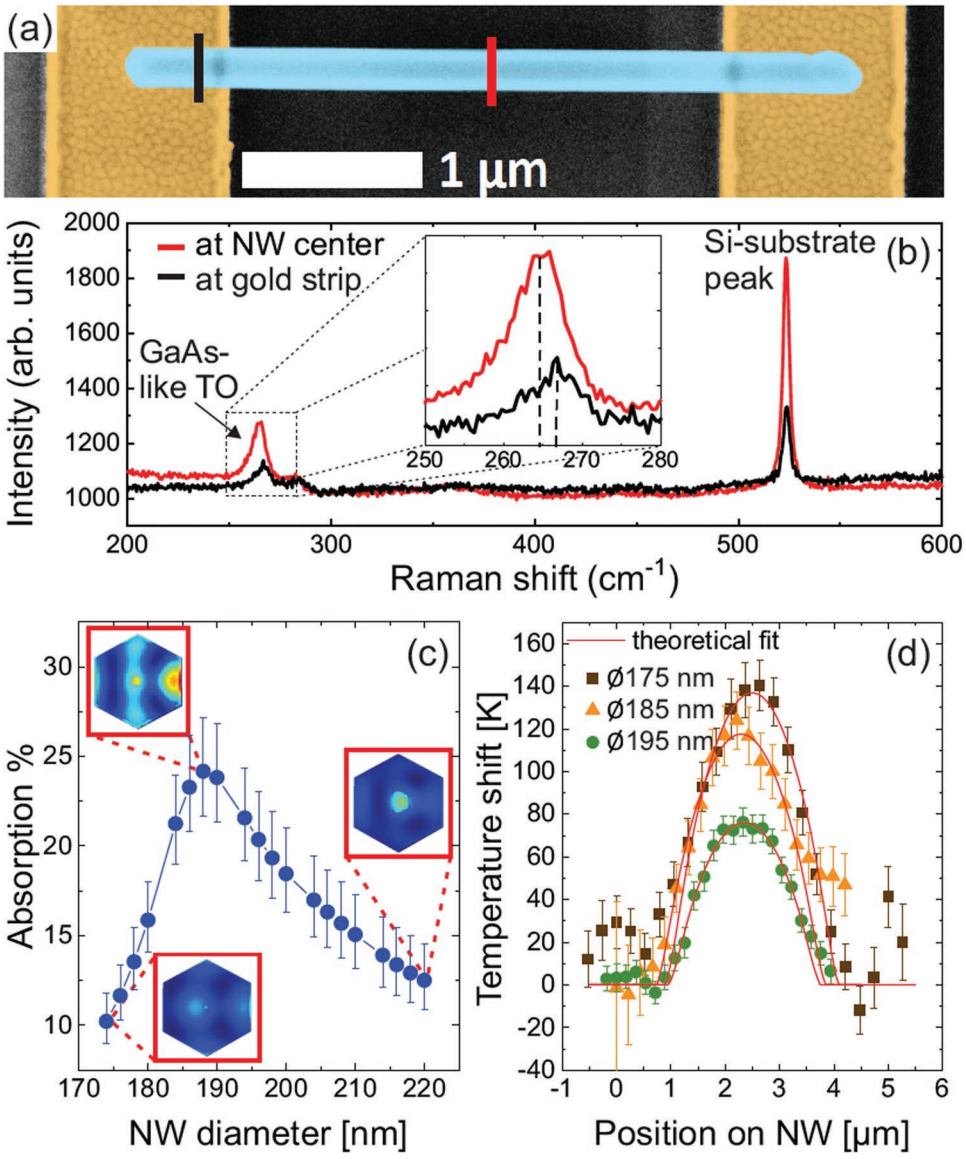

Figure 2. a) NW (blue) suspended on two 300 nm thick Au strips (spacing 3 µm) over a Si substrate. b) Respective Raman spectra for the NW locally heated and probed at the heat sink (black) and in the center region of the NW (red). The inset shows the shift of the GaAs-like TO peak due to the corresponding temperature increase. c) Fraction of laser-power absorbed by the NW as a function of the total NW diameter, as calculated using FDTD simulations. Here, the shell thickness is kept constant (80 nm), while the core diameter is swept from 15 to 60 nm, resulting in total NW diameters of ≈175–220 nm. The error bars take into account any potential changes in the laser beam diameter during the experiment. The insets show absorption profiles for different NW diameters. d) Temperature profile as a function of the position measured on the NW for three individual NWs, i.e., NW-1 (175 nm) and NW-2 (185 nm) probed for a laser-power of 100 µW, and NW-3 (195 nm) probed at 140 µW. Closed symbols refer to experimental data points, while the solid lines (red) are fits yielding the parameter $f = \kappa A/P_{abs}$. Error bars represent the uncertainty in position of the GaAs TO phonon peak.

pin down the dominant effects on phonon transport in these NWs.

To perform thermoelectric measurements, test structures were fabricated that consist of individual top-gated NW field effect transistors (NW-FETs) on SiO_2/n^{++}-Si substrate, as shown by the color-coded SEM image in **Figure 4**a. Hereby, the modulation-doped GaAs–AlGaAs core–shell NW is contacted in a two-terminal configuration (AuGe/Ni/Ti/Au source, drain contacts) and an omega-shaped Ti/Au top-gate wrapped around the NW channel with a gate length of ≈500 nm.[19] Note, the device shown in Figure 4a characterizes a ≈185 thick NW, similar to NW-2 that was presented in the previous section. The device also features two 4-point Ti/Au electrodes and meandering metal strip lines placed on each end of the NW which serve as local resistive thermometers and Joule heaters, respectively.[48] To induce a Seebeck voltage across a single NW, a temperature gradient ΔT was established by applying a heating power ($P = V_h^2/R_h$, $V_h = I_h R_h$ with V_h = heater voltage, I_h = heating current, R_h = resistance of heater) to one end of the NW, while the corresponding open-circuit thermovoltage was measured between the source and the drain contacts. ΔT was calibrated by recording the temperature-dependent

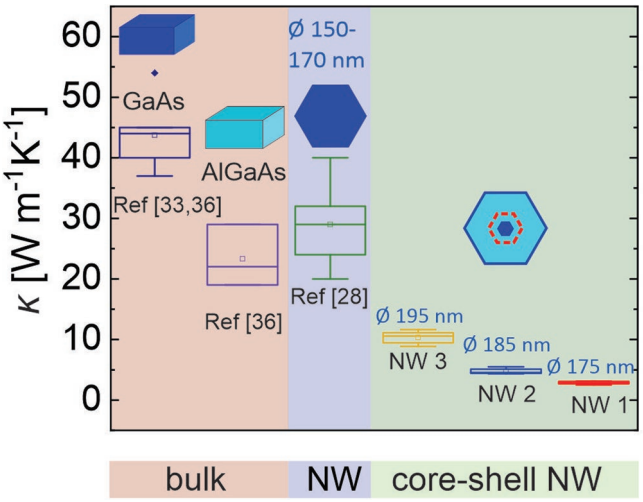

Figure 3. Summarized thermal conductivity data of representative GaAs–AlGaAs core–shell NWs at room-temperature, as measured in this work (green region). For comparison, the thermal conductivities for unpassivated GaAs NWs (purple region)[28] as well as for bulk GaAs and AlGaAs (orange region)[33,36] are also shown. Error bars for the core–shell NWs stem from statistical analysis based on multiple measurements on the same device.

resistance of the Ti/Au thermometers during a cool-down from 300 to 4.2 K, and additionally the resistance of the thermometers at several heater powers at 4.2 K. Direct comparison of the two data sets enables a good estimate of the induced ΔT. For example, at the highest heater power (P = 12 mW, see further below) the hot and cold ends are 12.5 and 8.2 K, respectively, resulting in $\Delta T \approx 4.3$ K. The distance between the thermometers is slightly larger than the distance between the NW ends, meaning that the real temperature gradient causing the Seebeck voltage might be lower (by <30%) than the one specified above, so that the extracted Seebeck coefficients represent a lower limit. All measurements were performed on dedicated chip-carriers (24-pin breakout) in a custom-made He-flow cryostat allowing temperature-variable measurements.

First, we describe electrical transport measurements, which were performed at a source–drain voltage V_{SD} of 2 mV and a gate voltage V_G swept between −2.5 and 0 V at a rate of ≈25 mV s^{-1}. We note that while at room temperature a very small hysteresis of ≈20 mV was present, the hysteresis vanished entirely at low temperature. In addition, during cool-down from 300 K to a final temperature of 4.2 K, the pinch-off voltage remains the same or reduces only slightly, hinting toward the existence of a confined electron gas.[19] The transfer curve as illustrated in Figure 4b, top, probed here for a modulation-doped NW with a ≈30 nm thick GaAs core, shows normally-on n-type FET characteristics with a pinch-off appearing at V_G of −2.2 V at 300 K and at $V_G \approx -1.9$ V at 4.2 K (see Supporting Information). The on-current I_{SD} at 4.2 K is around 20 nA, giving a total resistance of ≈100 kΩ (i.e., sum of NW and contact resistance). At low temperature, the major fraction of the device resistance stems from contact resistance, as confirmed by previous measurements on equivalent Si δ-doped GaAs–AlGaAs core–shell NW-FETs.[19] By contrast, the intrinsic NW resistance in such devices drops at low temperatures due to formation of a confined electron gas in the NW core channel.[19,22] Although the present device shows reasonable characteristics, we emphasize that the majority of devices exhibited even much larger contact resistances (i.e., I_{SD} of only few hundred pA even at 300 K) and, thereby, prohibited quantum transport characterization at low temperature.

Most importantly, in Figure 4b we recognize a nonlinear, stepwise increase with several plateaus in the source–drain current I_{SD} with increasing V_G, which is fully reproducible for several up- and down-sweeps. The measured I_{SD} was converted to conductance G through the NW by subtracting the resistance due to the contacts and other in-line resistances in the two-terminal device geometry.[22] When plotting the conductance G of the NW, the plateaus appear in a periodic manner indicative of quantized conductance in a quasi-1D system. Unlike in the ballistic regime, where the conductance plateaus occur at integer values of $2e^2/h$, the conductance plateaus observed here occur at lower G (electron transmission probabilities $T \approx 0.2$), illustrating a nonballistic, diffusive 1D transport regime.[7,22] Note that the very first plateau at $V_G = -1.83$ V deviates from this trend in that its step height is much lower, as further discussed below. Importantly, the observed steps can be directly associated with the discrete 1D sub-band nature, arising from the electron confinement in the NW core, with individual sub-bands being filled/depleted upon variation of V_G. In particular, the number of experimentally observed plateaus and corresponding step sizes (energy level spacings) are determined by the presence of occupied single and double degenerate states below the Fermi level for the given diameter of the core channel.[22] Here, we observe a total of five discrete occupied states at pinch-off for a core diameter of ≈30 nm. This is in good quantitative agreement with previous data obtained on equivalent modulation-doped GaAs–AlGaAs core–shell NWs with very similar core-diameter.[22] We further note that the conductance steps vanish for temperatures exceeding ≈10 K (see Supporting Information), which is expected due to increased thermal and disorder-mediated energy level broadening given the relatively small sub-band spacing in these NWs (<10 meV).[22] We believe that with substantially increased electron mobility disorder-mediated scattering could be reduced, thus, allowing observation of 1D-sub-band transport up to higher temperatures, as in, e.g., InAs NWs.[13,14]

Consecutive gate-dependent thermopower measurements performed on the same device at 4.2 K are depicted on the lower panel of Figure 4b, showing traces of the corresponding thermovoltage at four different heater powers (0.16–12.3 mW) applied to one of the two resistive heating elements. The thermovoltage was normalized to exclude stray potential differences arising in the experimental setup, by subtracting the Seebeck voltage at zero heater-power V_{S0} from the Seebeck voltage trace at the desired heater-power, i.e., $\Delta V_S = V_{SX} - V_{S0}$. The gate-dependent thermovoltage shows characteristic behavior; in particular, quantum oscillations with discrete maxima and minima characteristic of 1D sub-band transport are observed that are closely connected to the stepwise increase in the conductance G.[49–51] The positions of the peaks are independent of the applied heater power, i.e., the gate voltage values at which the oscillations occur are identical for gate sweeps at all temperature gradients. Qualitatively similar characteristics are also observed for thermopower measurements via the other heating element (see Supporting Information).

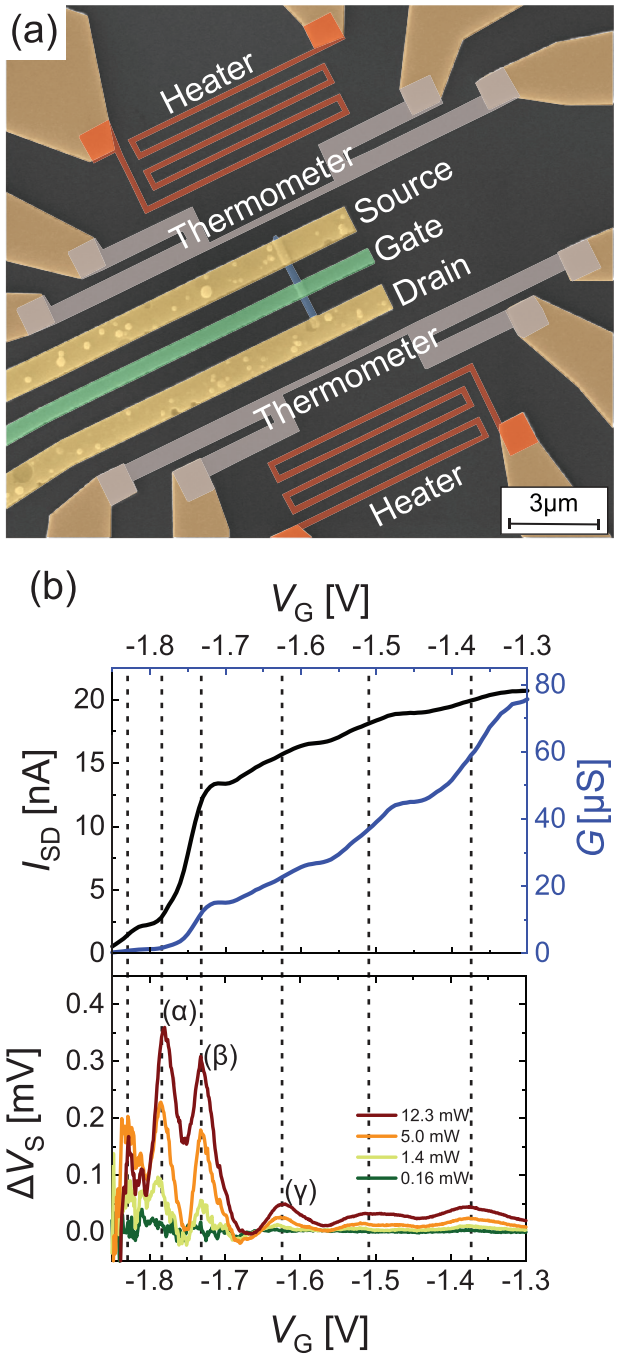

Figure 4. a) Color-coded SEM image of test structure used to investigate thermoelectric transport properties of individual modulation-doped GaAs–AlGaAs core–shell NWs. The NW (blue) is contacted by source/drain contacts (yellow) in a two-terminal configuration, with an omega-shaped top gate (green) placed in between. A Seebeck voltage is induced by applying a heating current to one of the two resistive meander heaters (red). The temperature gradient is observed by measuring the change in the resistance of the two line-thermometers (silver) placed at the NW ends. (b, top) Transfer characteristic at 4.2 K of an individual Si δ-doped GaAs/AlGaAs core–shell NW-FET plotted in I_{SD}–V_G and G–V_G (conductance) representation. (b, bottom) Corresponding Seebeck voltage (normalized) for heater powers of 0.16, 1.4, 5.0, and 12.3 mW as a function of V_G. The dashed lines show the V_G values at the thermopower peaks, which coincides with the corresponding plateau onset in the conductance G.

Overall, the most interesting feature is clearly the coincidence of each peak appearing in the Seebeck voltage with the onset of each step in the conductance trace. This correlation is expected due to the variation of the electron density of states, i.e., change in the number of occupied 1D sub-bands, which mimics closely the behavior observed in quantum point contacts (QPCs).[52,53] In other words, when the Fermi level (E_F) is within an energy range $\approx k_B T$ close to a sub-band edge, the Seebeck voltage rises (step in G), and drops again (plateau in G) when E_F is more than $\approx k_B T$ away from the sub-band edge. Since the energy spacings of the individual 1D sub-bands are at least several meV in the present NWs,[22] the thermal broadening $\approx k_B T$ is negligibly small and, thus, the observation of 1D sub-band quantization and the oscillating thermopower are validated. Moreover, our data shows that with decreasing V_G the height of the peak in the Seebeck voltage increases, as we move toward the lowest 1D-sub-band. Such behavior is expected as the peak height depends on the respective sub-band number N via $S \simeq -k_B/e \cdot \ln 2/\left(N-\frac{1}{2}\right)$.[53] While this trend is qualitatively well observed, however, the highest Seebeck voltage is not seen at $V_G = -1.83$ V, which is assumed to be the lowest sub-band, but at the second sub-band, i.e., $V_G = -1.78$ V. Additionally, for the lowest sub-band the Seebeck voltage saturates with increasing heating power, not following the same trend of the peak height-to-temperature gradient dependence as seen for higher sub-bands. Possible reasons for these observations might be inferred from the suppressed conductance step height at $V_G = -1.83$ V, which deviates from the much larger step heights seen for higher sub-bands. Such deviation could be induced if, e.g., the 1D-channel is not perfectly symmetric,[54] or a nonsymmetric electric field by the omega-gate slightly deforms the 1D electron gas—both leading to a broken rotational hexagonal symmetry.[7,55] Similar observations were also made on thin InAs NWs, e.g., Tian et al. reported the largest thermopower for the fourth 1D-sub-band[13] while Chen et al. found increased thermopower in the 3rd sub-band compared to the second sub-band.[7]

Knowing the temperature gradient for the different heater powers, the Seebeck coefficient was extracted from the amplitude of each peak via $S = -\Delta V/\Delta T$. The Seebeck coefficients for the first three pronounced peaks were −83, −66, and −11 μV K^{-1}, respectively (see **Figure 5**a). The sign of the Seebeck coefficient confirms the n-type nature of the Si δ-doped GaAs core channel, which is expected since the measured voltage gradient ΔV_S implies diffusion of a high density of electrons from the hot to the cold end, where they build up an increasingly negative potential. The values of the Seebeck coefficient extracted from the lowest 1D-sub-bands are quite large and compare favorably with those reported from other systems with 1D-sub-band quantization measured at comparable lattice temperature. For example, QPCs based on high-mobility GaAs/AlGaAs 2DEGs,[52,53] exhibit S values of ≈−20 to −40 μV K^{-1}, while for 1D-like InAs NWs a maximum value of S for the lowest 1D-sub-band was recently reported to be ≈ −100 μV K^{-1}.[7] Other reports on InAs NWs indicated much lower $S \approx -4$ μV K^{-1}, despite the fact that they were measured at higher temperatures, which tends to increase the Seebeck coefficient.[14,56]

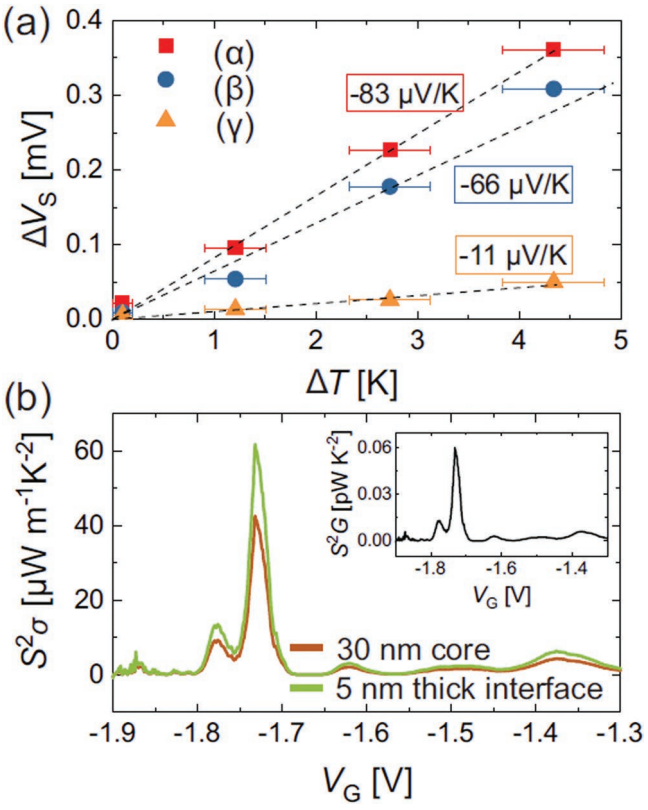

Figure 5. a) Seebeck voltage as a function of temperature gradient. The data points correspond to peak values in Seebeck voltage of the first three dominant oscillations at $V_G = -1.78$ V (red), −1.73 V (blue), and −1.62 V (yellow), respectively. Best fits to the data (dashed lines) provide quantitative values for the extracted Seebeck coefficients. b) Power factor for the case of the conductivity through a 30 nm thick NW core (brown curve), as well as a 5 nm thick interface region at the core–shell interface (green curve). The inset shows the power factor independent of the channel dimensions.

Finally, we provide estimates for the thermoelectric power factor, which we give in terms of S^2G as well as $S^2\sigma$ (see Figure 5b). As pointed out in refs. [7] and [57], for a mesoscopic 1D-channel S^2G as a measure for the thermoelectric power production is usually better suited, since describing electrical conduction locally is not fully appropriate in the quantum limit, where G becomes independent of device dimensions. As such, in a truly ballistic 1D-channel S^2G is considered as the maximum power factor, while S^2G also holds for nonballistic, diffusive 1D-channels under the Landauer formalism which takes the lower transmission probability into account.[7,58] From the data provided in Figures 4b and 5a for S and G, we obtain a maximum experimental value of $S^2G \approx 0.06$ pW K^{-2} for the third sub-band at $V_G = -1.73$ V while S^2G drops to below 0.01 pW K^{-2} for the neighboring sub-bands at $V_G = -1.78$ V (2nd sub-band) and $V_G = -1.62$ V (4th sub-band), as shown in the inset in Figure 5b. These values are comparable to the typical S^2G power factors measured in the first few sub-bands of other diffusive NWs, i.e., 1D-InAs NWs.[7] Compared to fully ballistic 1D-NWs, where the maximum feasible, i.e., universal power factor is $(S^2G)_{QB} = 0.73$ pW K^{-2} (so-called power factor quantum bound),[7,57] our experimental values are about one order of magnitude lower. Moreover, for our nonballistic 1D-NWs one can also delineate a diffusive upper limit, which is $(S^2G)_{QB}$ reduced by the transmission probability.[7] Taking the experimentally determined transmission probability of $T \approx 0.2$ (for gate length of 500 nm) into account, the diffusive power factor limit $(S^2G)_{limit}$ amounts, thus, to ≈0.14 pW K^{-2}.

In the limit of a fully diffusive transport regime, the equivalent $S^2\sigma$ was also calculated for transport within each sub-band. To obtain the equivalent electrical conductivity σ we assumed two limiting cases, i) where the electron density distribution spans across the entire GaAs-core cross-section (limiting case for ultrathin cores), and ii) the case where the electron density is concentrated within a ≈5 nm thin region near the GaAs–AlGaAs core–shell interface (for larger cores).[19,22] Hence, we obtain for the equivalent $S^2\sigma$ a maximum value again for transport in the third sub-band with $S^2\sigma \approx 40$ μW m^{-1} K^{-2} for the former case and ≈60 μW m^{-1} K^{-2} for the latter case (see Figure 5b). We suggest that the latter case is more realistic, since in modulation-doped GaAs/AlGaAs core–shell NWs with core diameter of >30 nm the electron density distribution in the third sub-band is, indeed, closely confined to the core–shell interface.[22] Since the description of thermopower by $S^2\sigma$ allows, in principle, to compare materials with different dimensionalities, it is tempting to benchmark our data with, e.g., bulk GaAs, for which investigations at low temperature are, however, scarce. Theoretical data obtained at 77 K and at optimized carrier density suggest a maximum achievable thermopower of ≈0.78 mW m^{-1} K^{-2} in n-type bulk GaAs.[59] As thermopower becomes, in general, even lower toward cryogenic temperatures and since the equivalent 3D carrier density in our present core–shell NWs deviates by about one order of magnitude from optimized doping density of reported bulk GaAs,[59] a direct quantitative comparison is not meaningful. Nevertheless, we expect improvements in thermopower of such 1D-confined NWs by adjusting doping density, while further reducing the cross-section of the 1D-core channel and increasing the electron mean free path, i.e., realizing NWs with higher mobility.[7]

In summary, we developed a promising model system for a 1D-quantum confined NW thermoelectric that enables both the observation of enhanced thermopower via quantum oscillations in the thermoelectric transport and a strong reduction in thermal conductivity induced by the core–shell heterostructure. High-mobility modulation-doped GaAs/AlGaAs core–shell NWs with a thin (sub-40 nm) GaAs core were employed in thermoelectric device test structures, where the electrical and thermoelectric transport was characterized on the same exact 1D-channel. 1D-sub-band transport at low-temperature was verified by a discrete stepwise increase in the conductance, which coincided with strong oscillations in the corresponding Seebeck voltage that decay with increasing sub-band number. Peak Seebeck coefficients as high as ≈65–85 μV K^{-1} were observed for the lowest sub-bands, resulting in equivalent thermopower of $S^2\sigma \approx 60$ μW m^{-1} K^{-2} and $S^2G \approx 0.06$ pW K^{-2} within a single sub-band. While the thermopower results are currently limited to the observation on a single NW device, further confirmation along with interesting new insights are expected from investigating modulation-doped GaAs–AlGaAs core–shell NWs tuned over a larger parameter space (e.g., variable core-diameter and sub-band-spacing, different doping densities, carrier mobilities,

and channel length). Remarkably, these core–shell NW heterostructures were also found to exhibit thermal conductivities as low as ≈3 W m^{-1} K^{-1}. These values are about one order of magnitude lower as compared to state-of-the-art unpassivated GaAs NWs, and are ascribed to effective phonon scattering induced by the core–shell geometry. These promising findings highlighted here clearly motivate future work that will adapt similar modulation-doped schemes to other materials systems. For example, high-mobility NW materials with intrinsically lower electron effective masses and, hence, larger 1D-sub-band splitting, such as selectively doped (In,Ga,Al)(As,Sb)-based core–shell NW heterostructures, are expected to further advance the field of 1D-NW thermoelectrics.

Experimental Section

Nanowire Growth: The NWs were synthesized in an all-solid-source Veeco GEN-II MBE system using standard effusion cells for Ga, and Al as well as a valved cracker source for supplying As_4. Si (111) wafers coated with a ≈20 nm thick SiO_2 layer were used as substrates, whereby the SiO_2 layer was etched wet-chemically (aqueous, dilute NH_4–HF solution) to a final thickness of ≈2 nm prior to growth. The thinned SiO_2 layer enables the formation of tiny pinholes in the SiO_2, which serve as nucleation centers for the epitaxial, i.e., vertical [111]-oriented growth of GaAs NWs.[23] First, VLS-type GaAs cores were grown for 1.5 h at a temperature T = 650 °C (as measured by optical pyrometer) using a Ga flux of 0.049 nm s^{-1} and an As beam equivalent pressure (BEP) of 4.2×10^{-6} mbar, respectively. This resulted in GaAs cores with length of ≈7–10 µm and diameter of ≈50–60 nm. Subsequently, the GaAs core was thinned by a so-called "reverse-reaction" growth (RRG) step, which includes an in situ thermal annealing step under ultrahigh-vacuum conditions (base pressure <10^{-7} mbar) with both Ga and As shuttered off.[23] This was performed on the as-grown NWs at 680 °C for 80 min, yielding a reduction in the core diameter to ≈25 ± 10 nm while the length also decreased to about ≈4–6 µm. The RRG step preserves the existing crystal phase and microstructure of the as-grown GaAs core.[23] In a final growth step, the radial modulation-doped AlGaAs shell structure with a nominal Al-molar fraction of 0.15 was grown at 490 °C, using a Ga flux of 0.17 nm s^{-1}, Al flux of 0.03 nm s^{-1}, and As-BEP of 3.5×10^{-5} mbar. After the first 20 nm of AlGaAs, the growth was halted and Si dopants were provided for 10 min under As-flux overpressure (δ-doped layer) using a thermal Si sublimation source with an equivalent heating current of 13 A. Afterward AlGaAs growth continued to create a 60 nm thick barrier layer, which was finally terminated by a ≈5 nm thin GaAs cap layer to inhibit oxidation of the AlGaAs shell.[60] A reference GaAs–AlGaAs core–shell NW sample was also grown under the same conditions for transmission electron microscopy analysis (Supporting Information), without thinning of the core and with a 10 nm thin undoped AlGaAs shell passivation layer.

Device Fabrication: Two sets of device structures were fabricated, i.e., one set for the electrical/thermoelectric transport characterization and another set for thermal transport measurements which employ µRaman spectroscopy. For test structures that involve thermoelectric transport characterization, NWs were stripped off mechanically from the native substrate and drop-casted onto an n^{++}-doped Si wafer coated with 200 nm thick SiO_2, which was prepatterned with 24 bond pads by optical lithography. Subsequently, the NWs were connected to the bond pads using standard electron beam lithography (EBL) and thermal evaporation. NWs were contacted for two-terminal sensing, with ohmic contacts acting as source and drain. As ohmic contacts AuGe/Ni/Ti/Au was used with layer thicknesses of 50/13.6/100/290 nm, respectively.[19,22] The contacts were further alloyed by annealing in an inert N_2 atmosphere at 400 °C for 105 s. According to recent experiments using identical contacting scheme, the contact resistance can be as low as ≈20–30 kΩ.[19,22] In a second step, an omega-shaped Ti/Au top-gate was placed symmetrically in between the source and drain, forming a Schottky barrier with the GaAs of around 0.8 eV.[61] To generate a temperature gradient along the NW and to further measure an induced thermovoltage, two resistive meandering heaters were implemented together with two thermometers at both NW ends to measure the corresponding temperature change. Both the thermometers and heaters were fabricated using the same Ti/Au metallization as the top-gate, however, their height was significantly reduced (≈50 vs ≈350 nm for the ohmic contacts and top-gate) to increase the sensitivity and the resistance, respectively. Likewise, the device structures for the µRaman spectroscopy measurements were fabricated in a similar manner using EBL and thermal evaporation directly on a native Si substrate. The prepatterned substrate consists, thus, of an array of 300 nm thick and 1 µm wide Au strips spaced 3 µm apart with markers to facilitate the search and recognition of suitable NWs. Using mechanical transfer, the NWs were randomly distributed on the prepatterned substrate, with few NWs bridging the Au strips. This way the suspended NWs were separated from the substrate, creating thermal contact only with the Au strips that act as heat sinks (thermal contact resistance being negligible).

Device Characterization and Simulation: To analyze thermal conductivity, µRaman spectroscopy was employed in backscattering geometry, where a He-Ne laser (wavelength 632.8 nm) was focused through a 63× objective lens with a numerical aperture of 0.75. The sample was placed in a vacuum chamber and a piezostage moves the sample under the laser beam, recording a spectrum at several discrete positions along the nanowire for a given time period. Raman spectra were collected with an XY Dilor triple spectrometer. The GaAs-like TO phonon peak was calibrated for maximum intensity at the NW center position by employing scans along a line perpendicular to the NW axis. The center was determined as the position where the intensity ratio between the GaAs TO-phonon peak to the Si substrate peak was the highest. Determination of thermal conductivity required numerical simulation of the absorbed Raman laser power by the NW using Lumerical FDTD simulations. The simulation was performed for NWs suspended 300 nm over the Si substrate, mimicking the experimental conditions. The NW diameters employed in the simulation ranged from 175 to 220 nm, while different laser beam radii between 634 and 892 nm were also taken into account in order to consider possible changes in the beam waist of the incident laser beam. The error bars in Figure 2c correspond to this variation in beam waist. Concerning electrical measurements, DC measurements were realized using a Yokogawa 7651 DC power source that supplies constant DC voltage to the source–drain contacts as well as for gating the NW. The resulting current at V_{SD} = 2 mV was measured using a Femto DLPVA-100-F-D, a DL 1211 current preamplifier and a Keithley 2000 digital multimeter. For measurements at cryogenic temperatures, the sample was placed in a custom-made He flow cryostat to perform measurements at 4.2 K. In addition, for thermoelectric characterization, the open-circuit voltage (thermovoltage) was measured using an Agilent 34420 A nanovoltmeter. A voltage of V_h = 1, 3, 6, and 10 V applied to the heater resulted in a heater power of 0.16, 1.4, 5.0, and 12.3 mW, respectively. For the actual temperature dependence of ΔV_S, the thermovoltage at zero heater-power V_{S0} was subtracted from the data with applied heater-voltage V_{SX}, in order to suppress the influence of the setup on the obtained data.

Supporting Information

Supporting Information is available from the Wiley Online Library or from the author.

Acknowledgements

The authors gratefully acknowledge H. Riedl for experimental support at the MBE system. This work was supported by the Deutsche Forschungsgemeinschaft (DFG, German Research Foundation) under Germany's Excellence Strategy–EXC 2089/1–390776260, and

the "Nanosystems Initiative Munich (NIM)." The authors further acknowledge support by DFG-projects KO4005/5-1, KO4005/6-1, as well as the International Graduate School of Science and Engineering (IGSSE) and the Institute for Advanced Study at the Technical University of Munich.

Conflict of Interest

The authors declare no conflict of interest.

Keywords

nanowires, quantum transport, Raman spectroscopy, thermal conductivity, thermoelectrics

Received: August 22, 2019
Revised: November 19, 2019
Published online: December 9, 2019

[1] A. Majumdar, *Science* **2004**, *303*, 777.
[2] D. M. Rowe, *Thermoelectrics Handbook: Macro to Nano*, CRC/Taylor & Francis, Boca Raton, FL **2006**.
[3] A. Bejan, A. D. Allan, *Heat Transfer Handbook*, Wiley, New York **2003**.
[4] L. D. Hicks, M. S. Dresselhaus, *Phys. Rev. B* **1993**, *47*, 12727.
[5] M. S. Dresselhaus, G. Chen, M. Y. Tang, R. Yang, H. Lee, D. Wang, Z. Ren, J.-P. Fleurial, P. Gogna, *Adv. Mater.* **2007**, *19*, 1043.
[6] L. D. Hicks, M. S. Dresselhaus, *Phys. Rev. B* **1993**, *47*, 16631.
[7] I.-J. Chen, A. Burke, A. Svilans, H. Linke, C. Thelander, *Phys. Rev. Lett.* **2018**, *120*, 177703.
[8] A. I. Boukai, Y. Bunimovich, J. Tahir-Kheli, J.-K. Yu, W. S. Goddard III, J. R. Heath, *Nature* **2008**, *451*, 168.
[9] A. I. Hochbaum, R. Chen, R. D. Delgado, W. Liang, E. C. Garnet, M. Najarian, A. Majumdar, P. Yang, *Nature* **2008**, *451*, 163.
[10] E. K. Lee, L. Yin, Y. Lee, J. W. Lee, S. J. Lee, J. Lee, S. N. Cha, D. Whang, G. S. Hwang, K. Hippalgaonkar, A. Majumdar, C. Yu, B. L. Choi, J. M. Kim, K. Kim, *Nano Lett.* **2012**, *12*, 2918.
[11] G. Zhang, B. Kirk, L. A. Jauregui, H. Yang, X. Xu, Y. P. Chen, Y. Wu, *Nano Lett.* **2012**, *12*, 56.
[12] A. C. Ford, S. Bala Kumar, R. Kapadia, J. Guo, A. Javey, *Nano Lett.* **2012**, *12*, 1340.
[13] Y. Tian, M. R. Sakr, J. M. Kinder, D. Liang, M. J. MacDonald, R. L. J. Qiu, H.-J. Gao, X. P. A. Gao, *Nano Lett.* **2012**, *12*, 6492.
[14] P. Mensch, S. Karg, V. Schmidt, B. Gotsmann, H. Schmid, H. Riel, *Appl. Phys. Lett.* **2015**, *106*, 093101.
[15] M. Scheffler, S. Nadj-Perge, L. P. Kouwenhoven, M. T. Borgström, E. P. A. M. Bakkers, *J. Appl. Phys.* **2009**, *106*, 124303.
[16] A. C. Ford, J. C. Ho, Y.-L. Chueh, Y.-C. Tseng, Z. Fan, J. Guo, J. Bokor, A. Javey, *Nano Lett.* **2009**, *9*, 360.
[17] M. Y. Swinkels, M. R. van Delft, D. S. Oliveira, A. Cavalli, I. Zardo, R. W. van der Heijden, E. P. A. M. Bakkers, *Nanotechnology* **2015**, *26*, 385401.
[18] Z. Wang, N. Mingo, *Appl. Phys. Lett.* **2010**, *97*, 101903.
[19] S. Morkötter, N. Jeon, D. Rudolph, B. Loitsch, D. Spirkoska, E. Hoffmann, M. Döblinger, S. Matich, J. J. Finley, L. J. Lauhon, G. Abstreiter, G. Koblmüller, *Nano Lett.* **2015**, *15*, 3295.
[20] T. Stettner, P. Zimmermann, B. Loitsch, M. Döblinger, A. Reler, B. Mayer, J. Winnerl, S. Matich, H. Riedl, M. Kaniber, G. Abstreiter, G. Koblmüller, J. J. Finley, *Appl. Phys. Lett.* **2016**, *108*, 011108.
[21] T. Stettner, A. Thurn, M. Döblinger, M. O. Hill, J. Bissinger, P. Schmiedeke, S. Matich, T. Kostenbader, D. Ruhstorfer, H. Riedl, M. Kaniber, L. J. Lauhon, J. J. Finley, G. Koblmüller, *Nano Lett.* **2018**, *18*, 6292.
[22] D. M. Irber, J. Seidl, D. J. Carrad, J. Becker, N. Jeon, B. Loitsch, J. Winnerl, S. Matich, M. Döblinger, Y. Tang, S. Morkötter, G. Abstreiter, J. J. Finley, M. Grayson, L. J. Lauhon, G. Koblmüller, *Nano Lett.* **2017**, *17*, 4886.
[23] B. Loitsch, D. Rudolph, S. Morkötter, M. Döblinger, G. Grimaldi, L. Hanschke, S. Matich, E. Parzinger, U. Wurstbauer, G. Abstreiter, J. J. Finley, G. Koblmüller, *Adv. Mater.* **2015**, *27*, 2195.
[24] C. Pöpsel, J. Becker, N. Jeon, M. Döblinger, T. Stettner, Y. Trujillo Gottschalk, B. Loitsch, S. Matich, M. Altzschner, A. W. Holleitner, J. J. Finley, L. J. Lauhon, G. Koblmüller, *Nano Lett.* **2018**, *18*, 3911.
[25] S. Birner, T. Zibold, T. Andlauer, T. Kubis, M. Sabathil, A. Trellakis, P. Vogl, *IEEE Trans. Electron Devices* **2007**, *54*, 2137.
[26] I.-K. Hsu, R. Kumar, A. Bushmaker, S. B. Cronin, *Appl. Phys. Lett.* **2008**, *92*, 063119.
[27] G. S. Doerk, C. Carraro, R. Maboudian, *Phys. Rev. B* **2009**, *80*, 073306.
[28] M. Soini, I. Zardo, E. Uccelli, S. Funk, G. Koblmüller, A. Fontcuberta i Morral, G. Abstreiter, *Appl. Phys. Lett.* **2010**, *97*, 263107.
[29] S. Yazji, M. Y. Swinkels, M. De Luca, E. A. Hoffmann, D. Ercolani, S. Roddaro, G. Abstreiter, L. Sorba, E. P. A. M. Bakkers, I. Zardo, *Semicond. Sci. Technol.* **2016**, *31*, 064001.
[30] I. Zardo, S. Conesa-Boj, F. Peiro, J. R. Morante, J. Arbiol, E. Uccelli, G. Abstreiter, A. Fontcuberta i Morral, *Phys. Rev. B* **2009**, *80*, 245324.
[31] Y. Zhang, Y. Sun, *16th Int. Solid-State Sens., Actuators & Microsystems Conf. Beijing 2011*, IEEE, Piscataway, NJ, USA **2011**, pp. 2582–2585.
[32] B. Jusserand, J. Sapriel, *Phys. Rev. B* **1981**, *24*, 7194.
[33] R. O. Carlson, G. A. Slack, S. J. Silverman, *J. Appl. Phys.* **1965**, *36*, 505.
[34] F. Zhou, A. L. Moore, J. Bolinsson, A. Persson, L. Froberg, M. T. Pettes, H. Kong, L. Rabenberg, P. Caroff, D. A. Stewart, N. Mingo, K. A. Dick, L. Samuelson, H. Linke, L. Shi, *Phys. Rev. B* **2011**, *83*, 205416.
[35] A. Weathers, A. L. Moore, M. T. Pettes, D. Salta, J. Kim, K. Dick, L. Samuelson, H. Linke, P. Caroff, L. Shi, *MRS Proc.* **2012**, *1404*, mrsf11-1404-w04-06.
[36] S. Adachi, *Properties of Aluminium Gallium Arsenide*, The Institution of Electrical Engineers, London **1993**.
[37] J. C. Duda, T. S. English, D. A. Jordan, P. M. Norris, W. A. Soffa, *J. Heat Transfer* **2012**, *134*, 014501.
[38] N. Jeon, B. Loitsch, S. Morkötter, G. Abstreiter, J. J. Finley, H. J. Krenner, G. Koblmüller, L. J. Lauhon, *ACS Nano* **2015**, *9*, 8335.
[39] T. Yao, *Appl. Phys. Lett.* **1987**, *51*, 1798.
[40] W. S. Capinski, J. J. Maris, T. Ruf, M. Cardona, K. Ploog, D. S. Katzer, *Phys. Rev. B* **1999**, *59*, 8105.
[41] R. Yang, G. Chen, M. S. Dresselhaus, *Nano Lett.* **2005**, *5*, 1111.
[42] M. Hu, X. Zhang, K. P. Giapis, D. Poulikakos, *Phys. Rev. B* **2011**, *84*, 085442.
[43] M. Hu, K. P. Giapis, J. V. Goicochea, X. Zhang, D. Poulikakos, *Nano Lett.* **2011**, *11*, 618.
[44] M. C. Wingert, Z. C. Y. Chen, E. Dechaumphai, J. Moon, J.-H. Kim, J. Xiang, R. Chen, *Nano Lett.* **2011**, *11*, 5507.
[45] A. K. Arora, M. Rajalakshmi, T. R. Ravindran, V. Sivasubramanian, *J. Raman Spectrosc.* **2007**, *38*, 604.
[46] D. L. Nika, A. I. Cocemasov, D. V. Crismari, A. A. Balandin, *Appl. Phys. Lett.* **2013**, *102*, 213109.
[47] J. Chen, G. Zhang, B. Li, *J. Chem. Phys.* **2011**, *135*, 104508.
[48] J. Becker, M. O. Hill, M. Sonner, J. Treu, M. Döblinger, A. Hirler, H. Riedl, J. J. Finley, L. J. Lauhon, G. Koblmüller, *ACS Nano* **2018**, *12*, 1603.
[49] P. Streda, *J. Phys.: Condens. Matter* **1989**, *1*, 1025.
[50] L. W. Molenkamp, H. van Houten, C. W. J. Beenakker, R. Eppenga, C. T Foxon, *Phys. Rev. Lett.* **1990**, *65*, 1052.
[51] N. J. Appleyard, J. T. Nicholls, M. Y. Simmons, W. R. Tribe, M. Pepper, *Phys. Rev. Lett.* **1998**, *81*, 3491.

[52] L. W. Molenkamp, T. Gravier, H. van Houten, O. K. A. Bujik, M. A. A. Mabesoone, C. T. Foxon, *Phys. Rev. Lett.* **1992**, *68*, 3765.
[53] H. van Houten, L. W. Molenkamp, C. W. J. Beenakker, C. T. Foxon, *Semicond. Sci. Technol.* **1992**, *7*, B215.
[54] M. M. Sonner, A. Sitek, L. Janker, D. Rudolph, D. Ruhstorfer, M. Döblinger, A. Manolescu, G. Abstreiter, J. J. Finley, A. Wixforth, G. Koblmüller, H. J. Krenner, *Nano Lett.* **2019**, *19*, 3336.
[55] A. Bertoni, M. Royo, F. Mahawish, G. Goldoni, *Phys. Rev. B* **2011**, *84*, 205323.
[56] S. Roddaro, D. Ercolani, M. A. Safeen, S. Suomalainen, F. Rossella, F. Giazotto, L. Sorba, F. Beltram, *Nano Lett.* **2013**, *13*, 3638.
[57] R. S. Whitney, *Phys. Rev. Lett.* **2014**, *112*, 130601.
[58] R. Kim, S. Datta, M. S. Lundstrom, *J. Appl. Phys.* **2009**, *105*, 034506.
[59] N. Mingo, *Appl. Phys. Lett.* **2004**, *84*, 2652.
[60] D. Rudolph, S. Funk, M. Döblinger, S. Morkötter, S. Hertenberger, L. Schweickert, J. Becker, S. Matich, M. Bichler, D. Spirkoska, I. Zardo, J. J. Finley, G. Abstreiter, G. Koblmüller, *Nano Lett.* **2013**, *13*, 1522.
[61] J. R. Waldrop, *Appl. Phys. Lett.* **1984**, *44*, 1002.